Applied Physics A (2023) 129:866
https://doi.org/10.1007/s00339-023-07134-7

Applied Physics A
Materials Science & Processing

NO_2 gas sensing performance of Ag–WO_{3-x} thin films prepared by reactive magnetron sputtering process

Modassar Hossain[1] · Krishnendu Sarkar[1] · Arnab Mondal[2] · Ankush Bag[3] · Probodh Kumar Kuiri[4] · Roopa[5] · M. Senthil Kumar[5] · Sandip Bysakh[1] · Prabir Pal[1]

Received: 21 August 2023 / Accepted: 4 November 2023 / Published online: 27 November 2023

Abstract
We have demonstrated a comparative study of NO_2 gas sensing behavior of reactive sputtered growth WO_{3-x} nanocrystalline thin films and its functionalization with Ag nanoparticles (Ag–WO_{3-x}) on Si/SiO_2 substrates. X-ray diffraction and transmission electron microscope characterizations demonstrate the formation of polycrystalline monoclinic phase of porous WO_{3-x} thin film. X-ray photoelectron spectroscopy experiments reveal that W^{6+} charge state has higher concentration compared with that of W^{4+} and W^{5+}. The Ag–WO_{3-x} films exhibit a sensitivity of about 70% at 10 ppm, while WO_{3-x} films show 12%, measured at 225 °C with same NO_2 gas concentration. The response and recovery time are 2 and 3 min. for Ag–WO_{3-x} films, while these for WO_{3-x} films are 3 and 4 min., respectively. This work shows that nano-scale dendritic agglomeration growth of Ag nanoparticles on WO_{3-x} surface can increase active sites for NO_2 gas and play an important role in trace-level gas sensing performance.

Keywords NO_2 gas sensing · Magnetron sputtering · Ag-decorated WO_{3-x} · Trace-level sensitivity

1 Introduction

Nitrogen dioxide (NO_2), mainly produced by the combustion of fossil fuels and automobile exhaust, is one of the most toxic air pollutants in the environments. The presence of NO_2 gas in the ambient atmosphere greater than 3 ppm (part per million) level concentration for a long span of time causes many environmental and health-related problems like acid rain, photochemical smog, air pollution, respiratory-related diseases, and cardiovascular diseases and reduces vegetation growth and crop yield. As per U. S. environmental protection agency, only 53 ppb (part per billion) level of NO_2 gas is considered to be as annual threshold limit. NO_2 is one of the most widespread toxic gases in the atmosphere, which is released from both indoor and outdoor activities. It is, therefore, important to monitor the concentration of this gas in the environment constantly in an economic way. This leads to fabricate a NO_2 sensing device which can work at atmospheric temperature continuously, i.e., without any applied external heating for economically sustainable. Therefore, superior gas sensing devices are essential for real-time air quality monitoring at the trace-level concentrations (ppb level) of NO_2.

The trace-level detection of NO_2 with superior selectivity and their material synthesis process via a cost-effective approach is still a major challenge. Recently, a lot of attention has been focused on metal-oxide (MOX) semiconductor nanostructure materials for various gas sensing performances due to their importance as trace-level detection, high sensitivity, fast response and recovery time, low energy consumption, and ease of operation [1–3]. One of the requisites for the superior sensitivity and selectivity for sensing is active surface area available at the surface and/or surface-interface morphology which affects the sensing performance

✉ Prabir Pal
prabir.p@cgcri.res.in

1 CSIR-Central Glass and Ceramic Research Institute, 196, Raja S. C. Mullick Road, Kolkata 700032, India

2 School of Computing and Electrical Engineering, Indian Institute of Technology Mandi, Mandi 175005, Himachal Pradesh, India

3 Department of Electronics and Electrical Engineering, Indian Institute of Technology Guwahati, Guwahati, India

4 Department of Physics, Sidho-Kanho-Birsha University, Purulia 723104, West Bengal, India

5 CSIR-National Physical Laboratory, Dr. K.S. Krishnan Road, New Delhi 110012, India

[4]. Among many MOXs, semiconducting WO_3 in different microstructural forms have been widely reported due to their superior and impressive characteristics, such as high surface-to-volume ratio, low carrier recombination time, and high chemical and thermal stability, which are the primary requirements for a gas sensing material [5] Akiyama et al. have shown that resistive type sensors using WO_3 are highly sensitive to NO and NO_2 [6]. However, bulk WO_3 requires high operating temperature and provides low selectivity, which potentially hinders its application in efficient sensing. To overcome these challenges and to improve the gas sensing performance of WO_3, nanostructured WO_3 has been utilized and various additional techniques have been demonstrated like doping, hybridization, and functionalization of WO_3 [7–9]. Functionalization with the noble metals is a well-established strategy to improve the gas sensing performance [10–14]. The relevant mechanisms for NO_2 gas sensing performance due to noble metal functionalization include better surface adsorption, electronic sensitization effect of constructing a metal–semiconductor contact, chemical sensitization effect, and the spillover effects. Typically, noble metals for their catalytic activities can decrease the absorption activation energies of gases on the surfaces of metal oxides resulting to an enhanced adsorption and sensing activities of MOX based sensors. The surface doping of nanosize clusters of noble metals may also enhance the active surface sites that facilitate the preferred adsorption of target gases and thereby increase their concentration to maximize the selectivity. Moreover, nanosize metallic clusters offer reaction paths that can reduce the activation energy and improve the reaction rate and, therefore, the selectivity, sensitivity, and reliability of the sensor.

Nanostructured Ag has been utilized very often with WO_3 to enhance its sensing characteristics. Chen et al. have demonstrated that the structural synergy between Ag and WO_3 is favorable for high-sensitivity NO_x sensing [15]. Wang et al. have investigated the enhanced NO_2 sensing performance of Ag-loaded mesoporous WO_3 synthesized in an ordered structure using three-dimensional hard cubic mesoporous silica (KIT-6) template. The authors demonstrated that the improved sensing using Ag-loaded WO_3 is dependent on the molar ratio of Ag loading. However, synthesis of mesoporous WO_3 involves an additional procedure of synthesis of hard template, which turns out to be complicated process [16]. Jaroenapibal et al. have demonstrated the improvement of NO_2 sensing performance of electrospun WO_3 nanofibers matrices with Ag doping [14]. The authors have demonstrated that the highest gas response in doped WO_3 nanofibers can be achieved at a specific Ag-doping level [16]. In spite of commendable NO_2 gas sensitivity and selectivity, sample preparation comprises three consecutive steps, viz., electrospinning, hot pressing, and calcination, which complicates the sensor fabrication [14]. Besides, a controlled decoration of Ag nanostructures on the surface of the sensing material is not possible in *in situ* chemical synthesis, because, in that case, a major portion of the added Ag is incorporated to the bulk of the material compromising its availability on semiconductor surface. Therefore, there is a necessity for advanced process to have controlled decoration of Ag nanostructures only on the MOX surface.

We have reported the effect of Ag nanoparticles on gas sensing mechanism toward NO_2 gas of WO_{3-x} nanocrystalline thin films prepared by reactive sputtering process followed by a precision coating technique to prepare Ag-functionalized surface. In the relevant literature, only a very limited work has been reported on the effect of novel metal decorated on metal-oxide nanostructure films for NO_2 gas detection using sputtering techniques. It was observed that there is an enhancement in the sensitivity of the gas sensor after decoration with Ag nanoparticles compared to the bare nanostructure films. The response and recovery time are also improved significantly in the Ag-decorated WO_{3-x} films at sufficiently low working temperature (225 °C).

2 Experimental details

The WO_3 thin films were prepared on Si/SiO_2 substrate by DC reactive magnetron sputtering using mixed gases of argon and oxygen (9:1) followed by an in situ post annealing in oxygen environment (25 sccm) at 700 °C for 2 h in the growth chamber. Prior to loading into the growth chamber, the substrates were cleaned step-by-step with trichloroethylene, acetone, and isopropyl alcohol, respectively, and then dried with nitrogen gas. Further cleaning was done by degassing the substrates at 550 °C for 3−4 h inside the growth chamber. A high purity 2″ metallic W (99.99%) was used as the target material for the growth process. The growth chamber with a base vacuum of ~ 4.0×10^{-6} mbar was achieved using a turbo molecular pumping system. Substrate temperatures were kept at 500 °C and applied DC power was fixed at 40 W for the growth process. The growth of the films was continued for 50 min and the thickness was estimated to be ~ 350 nm. After deposition, the films were functionalized with Ag nanoparticles using argon ion-beam sputter coating system (Gatan Precision etching and coating system (PECS), GATAN Inc. USA) in a base vacuum of ~ 10^{-3} mbar. During the growth, we kept equal current flow of ~ 444 µA from the two argon ion guns and the incident argon ion-beam power was set at 9 kV. The silver growth was done for 7 s at a deposition rate of ~ 3 Å/sec and the thickness was estimated to be ~ 2 nm. A post-deposition heat treatment was performed in an external tubular furnace at 500 °C for 30 min at 80 sccm argon flow to decorate Ag nanoparticles on WO_3 surface.

X-ray diffraction (XRD) patterns of WO_3 and Ag–WO_{3-x} samples were acquired using a X-ray diffractometer with Cu K_α radiation ($\lambda = 1.5418$ Å) in the 2θ range of 20–70° at a scanning rate of 0.05° s^{-1}. A transmission electron microscope (TEM) (Model no. Tecnai G^2 30 Super Twin) equipped with a charge couple device (CCD) camera from Gatan, Inc. USA, operating at 300 kV (FEI, The Netherlands), was used for TEM imaging. Cross-section TEM specimens were prepared by sandwiching two pieces of 2.5 mm × 10 mm-sized film-coated substrates with films face-to-face and mounted inside a 3 mm-diameter stainless steel tube with Gatan G1 epoxy and subsequently sectioning by Buehler precision diamond saw to obtain 3 mm-diameter, 0.25 mm-thick disc specimens of sectioned film-substrate sandwich. The sectioned discs were grinded down to 100 µm thickness, dimpled grinded to 20 µm thickness at disc center, and finally, argon ion-beam polishing was applied to obtain electron transparency of the film-substrate cross-section for TEM observation. The surface morphology and grain sizes were investigated using Field Emission scanning electron microscopy (FESEM) with energy-dispersive X-ray spectroscopy (EDX) (Sigma Carl Zeiss). Raman measurements were performed using a micro-Raman spectrometer (LabRAM HR, Jobin Yvon) equipped with an argon ion laser (488 nm) and a Peltier cooled CCD detector. The chemical composition and electronic structure of the as-prepared films were studied by X-ray photoelectron spectroscopy (XPS) (PHI 5000 Versa Probe II) with an incident Al Kα X-ray of energy 1486.6 eV. The binding energy for all measurements was calibrated by measuring C 1 s core-level spectra located at 286.7 eV. Total energy resolution was about 400 meV for monochromatic Al K_α excitation with pass energy of 11.750 eV.

The gas sensing measurements were performed by fabricating a suitable device with the prepared WO_{3-x} and Ag–WO_{3-x} films of substrate size approximately 5 mm × 5 mm. A shadow mask was used to make the interdigitated electrical contacts on the films, where 10 nm Ti upon which 90 nm Au was deposited using ion-beam sputter coating to make the contact pads. A home-built test setup was used to perform the gas sensing measurements. A Keithley source meter unit (2410) integrated with LabVIEW data acquisition software was utilized to measure the change in resistance upon exposure of the target gas at a constant bias voltage across the electrodes fabricated on the films surface. The electrical contacts on thin films were established using high-quality silver paint for the current–voltage (I–V) measurements. A linear I–V characteristic was obtained indicating a good ohmic nature of the fabricated electrical contacts. Calibrated NO_2 gas was used to investigate the gas sensing performances of WO_{3-x} and Ag–WO_{3-x} thin film sensors. The data of fabricated gas sensors were recorded at different operating temperatures (100–225 °C) and various gas concentrations (0.5–20 ppm) to test the sensitivity of the sensors.

3 Results and discussion

3.1 Characterizations of the films

Figure 1 shows the XRD data of WO_{3-x} and Ag–WO_{3-x} films taken at room temperature. All the sharp, intense XRD peaks of the films were identified using JCPDS no. 01-089-4476, suggesting the formation of a non-stoichiometric $WO_{2.82}$ monoclinic phase. A strong (002) peak observed at 23.1° is the characteristic feature of highly oriented crystalline films. However, no peaks corresponding to Ag were observed in the diffraction pattern possibly due to its very small layer thickness (~ 5 nm). The lattice parameters of the monoclinic $WO_{2.82}$ phase are found to be $a = 5.620$ Å, $b = 7.523$ Å, $c = 7.693$ Å, $\alpha = \gamma = 90°$, and $\beta = 99.41°$ from their refinement using Full Prof software and are found to be comparable with standard JCPDS data. The average crystal size of $WO_{2.82}$ has been determined using the well-known Scherrer relation [17]

$$\tau = \frac{K\lambda}{\beta\cos\theta}, \tag{1}$$

where τ is crystallite size, K is shape factor (i.e., 0.9), θ is Bragg's angle in degrees, β is full width at half maximum value of intensity (FWHM), and λ is the X-ray wavelength. The observed average crystallite size for (002) oriented peak remains same for both the samples and estimated to be about ~ 5 nm.

Figure 2a and b displays the FESEM images of WO_{3-x} and Ag–WO_{3-x}, respectively. The images show the nanostructure morphology with closed packed agglomerated grains of different orientations of average size around ~ 64 nm in diameter for bare films. While a finer

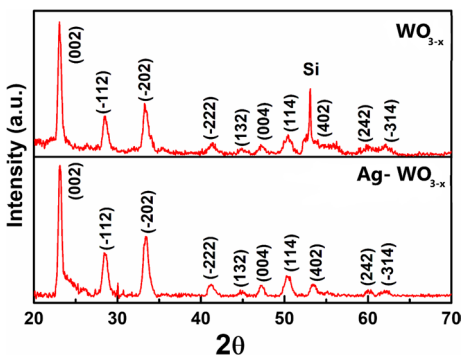

Fig. 1 Room-temperature X-ray diffraction measurements of monoclinic WO_{3-x} (top) and Ag–WO_{3-x} films (bottom) are shown

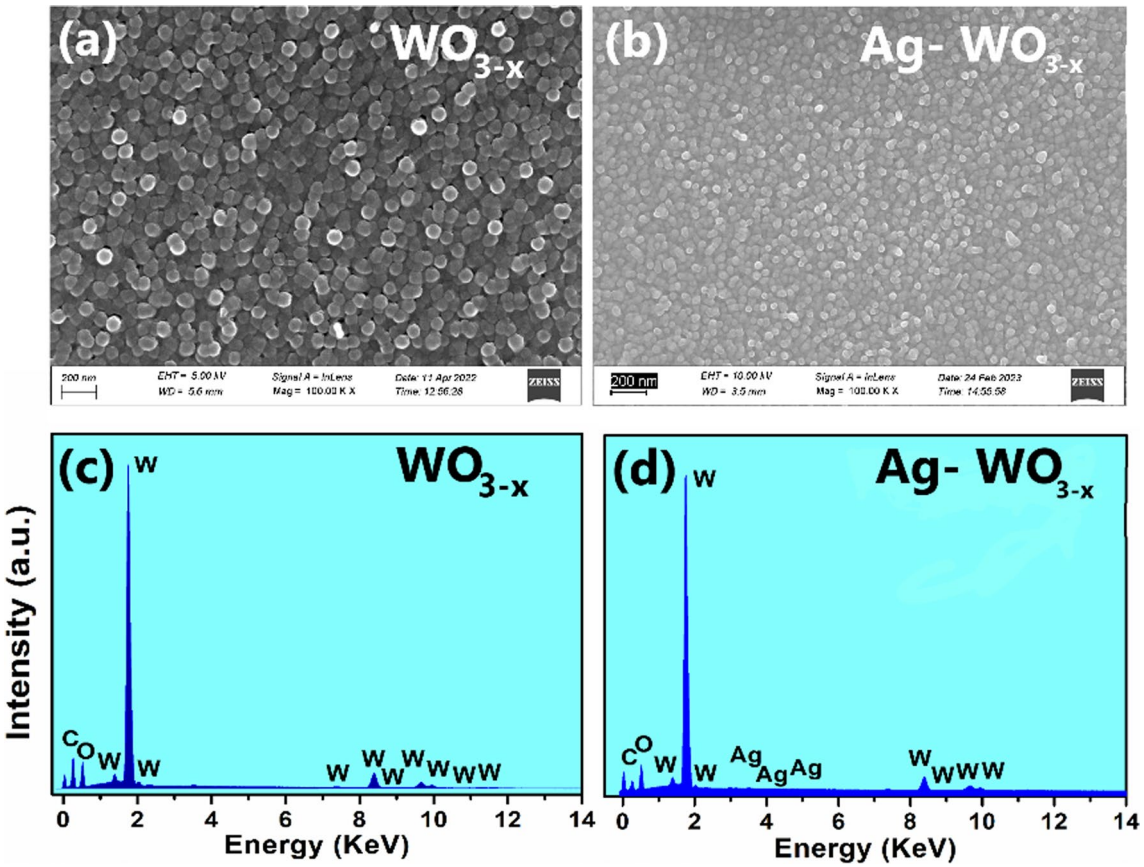

Fig. 2 FESEM images of **a** nanostructured WO_{3-x} and **b** Ag−WO_{3-x} thin films deposited on Si/SiO_2 substrates; **c** and **d** EDX signals of the respective samples

average grains of size about 35 nm was obtained with a higher number of grain boundaries for silver loaded film. The Ag nanoparticles are merely visible on the micrographs. Figure 2c and d presents the EDX measurements showing the presence of W, O, and Ag in the films. The finer details of film microstructures and crystallinity were investigated using transmission electron microscopy (TEM). Cross-sectional sample specimens were prepared for these investigations. The bright-field image of the film cross-section shows the growth of WO_{3-x} upon the amorphous SiO_2 layer of the substrate and the WO_{3-x} film thickness of about ~ 350 nm is observed in Fig. 3a. The image has also revealed the formation of fine nano-porosity along the grain boundaries as well as fine spherical nano-pores within the nanocrystals. The characteristic selected area electron diffraction (SAED) pattern obtained from the film is shown in Fig. 3b, which displays the diffraction rings, confirming the formation of polycrystalline nature of the WO_{3-x} monoclinic phase. The *d*-spacing values corresponding to the rings were calculated from the diffraction pattern and indexed using reference XRD data. The HRTEM image in Fig. 3c shows lattice fringes of two adjacent but differently oriented WO_{3-x} nanocrystals grown on the amorphous SiO_2 substrate. The observed lattice fringes in HRTEM images are indexed by their respective *d* values. The lattice fringes with a separation of 0.38 nm are observed indicating (002) planes, while 0.31 nm are observed for (− 112) planes of WO_{3-x} nanocrystals. Both the bright-field and HRTEM images show good adherence of the WO_3 film with the SiO_2 substrate layer. The bright-field TEM image of cross-section view of the WO_{3-x} film functionalized with Ag nanoparticles is shown in Fig. 4. The Ag nanoparticles are mostly spherical in shape and are about 5–8 nm in size range adhering to the WO_{3-x} surface as presented in Fig. 4b. The HRTEM investigations were carried out to view the crystallinity of the Ag nanoparticles present in the film. The crystal planes of Ag and WO_3 film are observed in the HRTEM image as presented in Fig. 4c. The image shows a clear lattice fringes with a separation of 0.23 nm for (111) planes of Ag nanoparticles as marked in the figure. The SAED pattern reveals the polycrystalline nature of the Ag nanoparticles' formations. The surface functionalized with Ag nanoparticles has more grain boundaries compared to

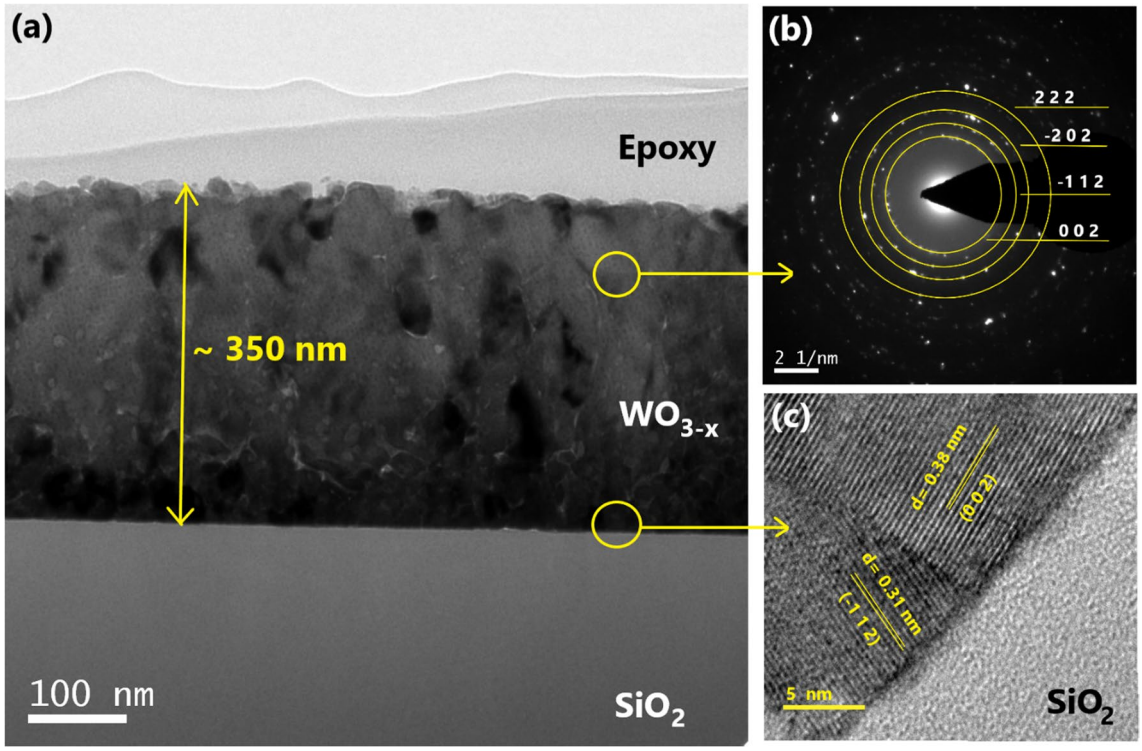

Fig. 3 **a** Cross-sectional bright-field TEM image showing the thickness of the WO_{3-x} film of around 350 nm. **b** SAED patterns of different crystallographic planes. **c** High-resolution (002) and (-112) orientation planes with corresponding interplanar distance of ~ 0.38 and ~ 0.31 nm, respectively

the bare films and it has more surfaces to volume ratio, which gives us additional active sites for oxygen ions on the surface of the films, and thereby significantly improving its sensing performance.

The Raman spectroscopy provides very useful information about the WO_3 films. Figure 5a shows the Raman spectra of WO_{3-x} and Ag–WO_{3-x} films taken in the same experimental conditions. The spectra exhibit four prominent peaks at 270, 303, 710, and 808 cm^{-1} derived from the lattice vibrations of the Raman characteristic peaks of the films. A detailed discussion on these Raman peaks can be found elsewhere [18]. As one can see from the figure, the intensities of the peaks obtained from Ag–WO_{3-x} film are less compared with those exhibited by the bare film. The intensity variations observed in the Raman characteristic peaks could be due to the presence of Ag nanoparticles. To investigate the effect of Ag nanoparticles in WO_{3-x} film, we have fitted the region from 550 to 900 cm^{-1} by Gaussian function for a comparison. The fitted spectra of bare and Ag–WO_{3-x} films are shown in Fig. 5b, c, respectively. There are five vibrational modes in the above region. The positions and full widths at half maximum (FWHMs) of the five peaks are given in the caption of Fig. 5. The peaks do not show any substantial shifts in positions as well as in the FWHMs as we go from bare to Ag nanoparticles loaded film. This indicates that no bond formation has taken place at the interface between WO_{3-x} and Ag nanoparticles.

The detailed XPS analysis has been carried out to determine the surface chemical compositions and oxidation states of the grown films. Figure 6a displays the XPS survey spectra of both the films. All the elements present in the films are marked in the figure in addition with adventitious carbon contaminations. Figure 6b, e shows the W 4f doublet peaks of main spin-orbital components obtained from WO_{3-x} and Ag-loaded films centered at 35.2 (W $4f_{7/2}$) and 37.4 eV (W $4f_{5/2}$), respectively, which are from W–O bonds of W^{6+} oxidation states. The main oxidation states is W^{6+} charge states, although small amount of W^{5+} and W^{4+} charge states are visible in both the films. In addition to that, a prominent W $5p_{3/2}$ located at ~ 41.1 eV was also observed. To estimate the relative percentage of three oxidation states, we have carefully fitted the W 4f spectra using χ^2 iterative program, keeping spin–orbit splitting and widths same for two samples. The details results obtained from fitting are shown in Table 1. The relative percentage of W^{4+}, W^{5+}, and W^{6+} charge states are calculated to be around 10.2, 17.5, and 72.2% for WO_{3-x} and 7.9, 21.8, and 70.3% for Ag–WO_{3-x} film, respectively. Figure 6c, f show the O 1 s core-level spectra deconvoluted with two features for both WO_{3-x} and Ag-loaded films, respectively. The main peak in O 1 s core

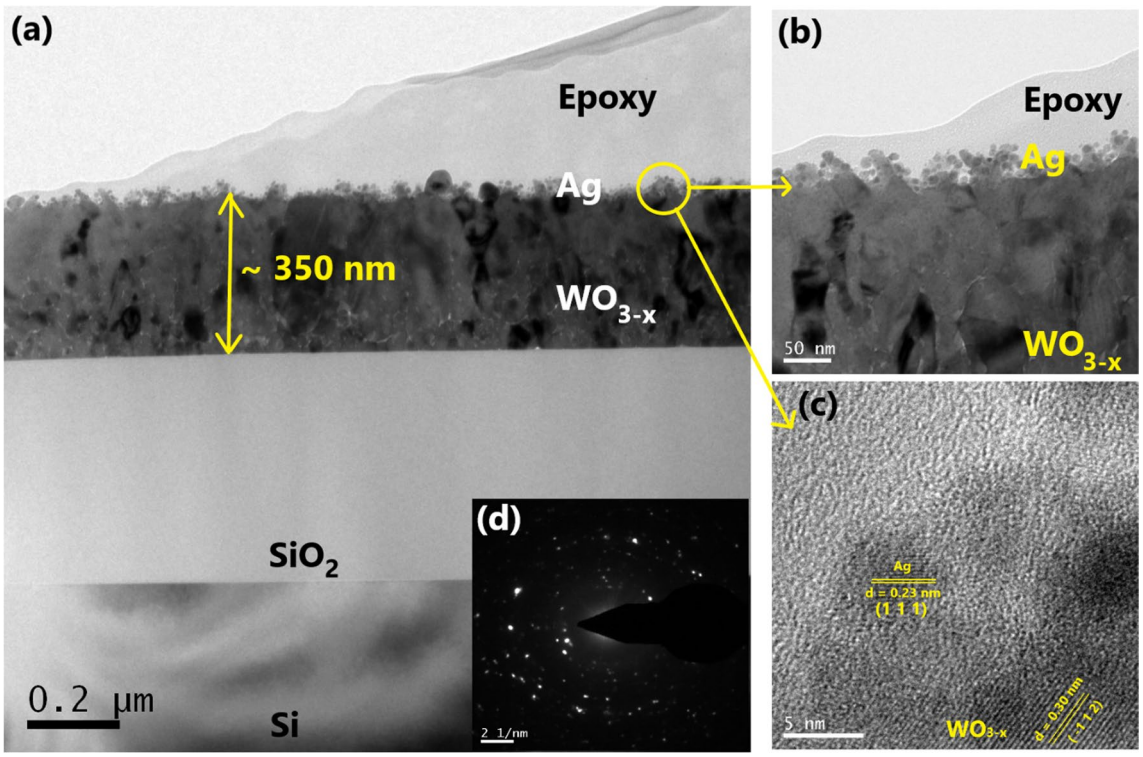

Fig. 4 **a** Cross-sectional bright-field TEM image of Ag nanoparticles loaded WO_{3-x} film. **b** Zoomed region showing the Ag nanoparticles are distributed over the WO_{3-x} nanocrystals film. **c** High-resolution Bragg planes taken from both WO_{3-x} film and Ag nanoparticles which are oriented along (-112) and (001) with 0.31 and 0.23 nm interplanar distances. **d** Inset of **a** shows the SAED image of the film

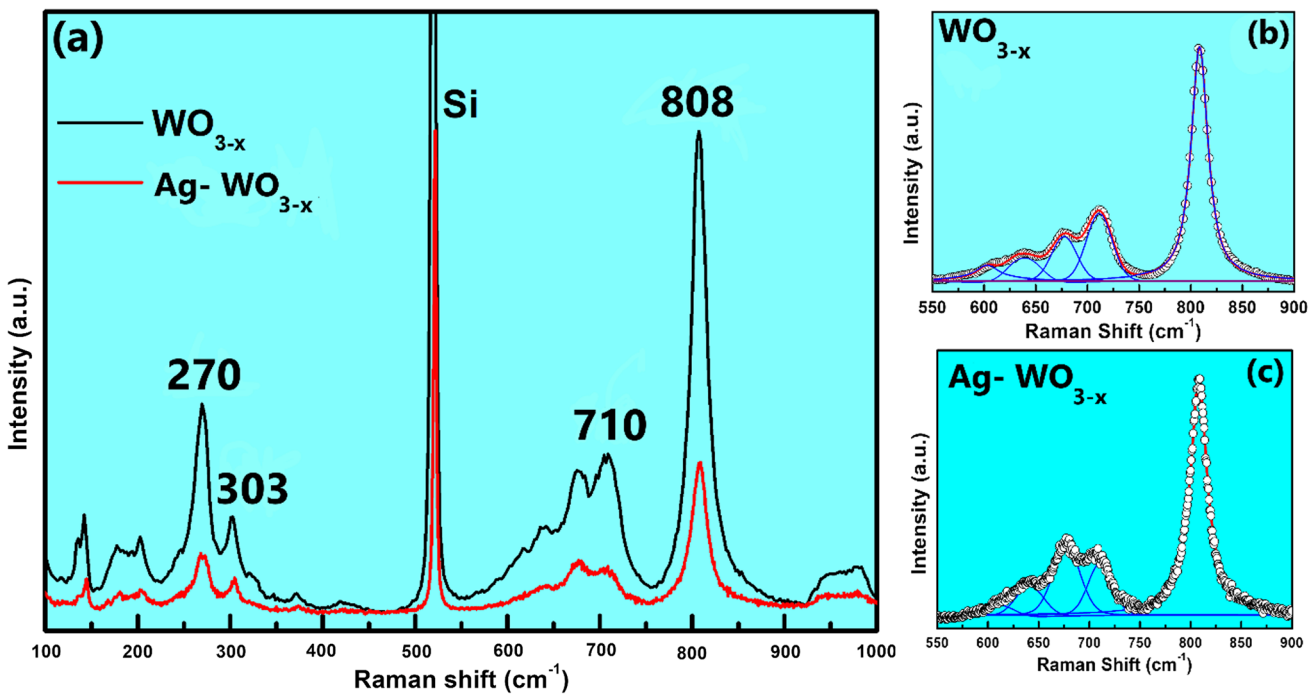

Fig. 5 **a** Raman spectra of WO_{3-x} and $Ag-WO_{3-x}$ thin films, taken using 488 nm laser source, which has all the four characteristics peaks present at 270, 303, 710, and 803 cm^{-1}, respectively; **b** and **c** fitted data of both the films from 550 to 900 cm^{-1} to observe the change in the spectra with silver nanoparticles decorated in WO_{3-x} film

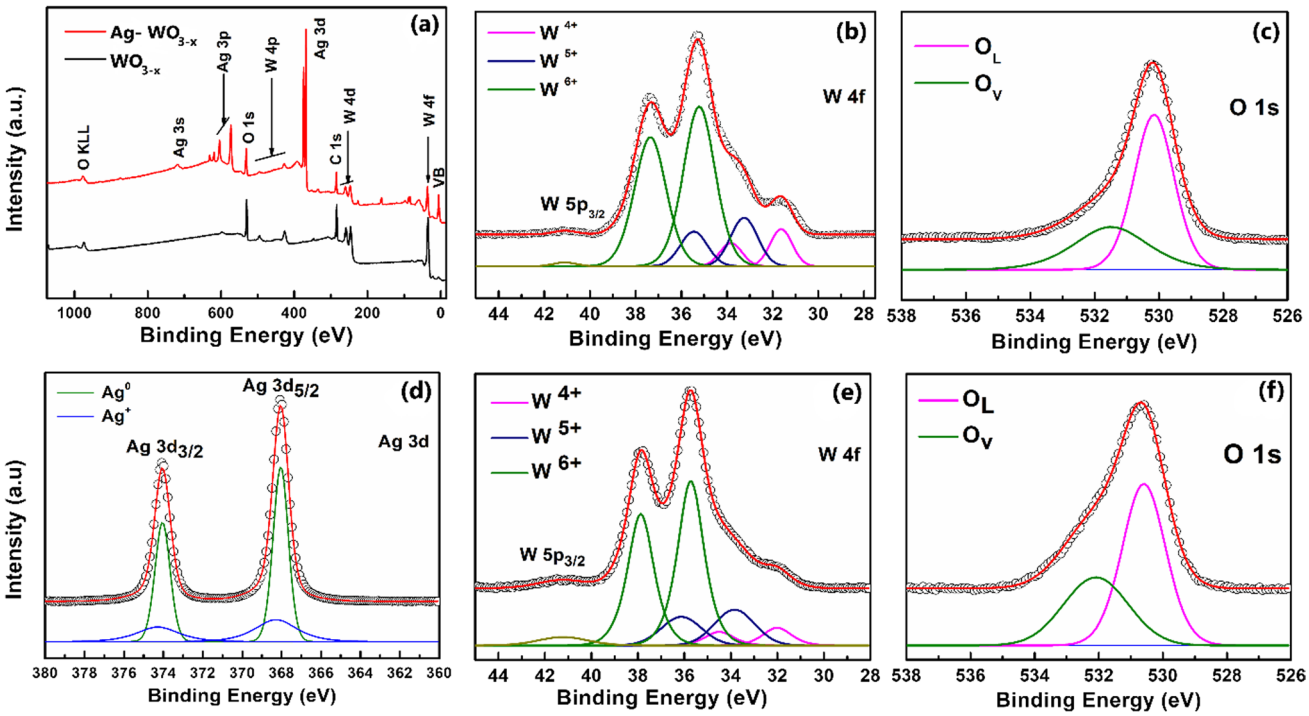

Fig. 6 **a** Survey spectra taken from WO_{3-x} (black line) and Ag–WO_{3-x} (red line) films. All the characteristics elements are present in both the films; **b** and **c** W 4f and O 1 s core-level XPS spectra (open circles) taken from WO_{3-x} films, respectively. Fitted spectra (solid red line) and different components used to fit each core-level spectra are also shown. The different charge states W^{4+}, W^{5+}, and W^{6+} are shown with violet, blue, and green lines, respectively. **d–f** Ag 3d, W 4f, and O 1 s core-level spectra taken from Ag–WO_{3-x} film, respectively. Small amount of Ag^+ charge state (blue) was formed along with Ag nanoparticles (green)

Table 1 Fitting parameters for the W 4f core-level spectra

Samples	W 4f								
	W $4f_{7/2}$ (W $4f_{5/2}$)								
	W^{4+} (W^{4+})			W^{5+} (W^{5+})			W^{6+} (W^{6+})		
	Position (eV)	FWHM (eV)	Normalized area	Position (eV)	FWHM (eV)	Normalized area	Position (eV)	FWHM (eV)	Normalized area
WO_{3-x}	31.6 (33.8)	1.14 (1.14)	6.3 (3.9)	33.2 (35.5)	1.40 (1.40)	10.3 (7.2)	35.2 (37.4)	1.63 (1.63)	39.9 (32.3)
Ag–WO_{3-x}	32.1 (34.3)	1.26 (1.26)	4.4 (3.5)	33.7 (35.9)	1.53 (1.53)	12.1 (9.7)	35.7 (37.9)	1.65 (1.65)	39.1 (31.2)

The binding energy positions, FWHMs, and normalized area of W^{4+}, W^{5+}, and W^{6+} species are listed. The normalized peak area of W^{4+}, W^{5+}, and W^{6+} specieswere found to be 10.2, 17.5, and 72.2% for WO_{3-x} and 7.9, 21.8, and 70.3% for Ag–WO_{3-x} film, respectively. We have used an integral background, which was kept identical for both the samples. Uncertainty in determining the binding energy position and FWHM is found to be ± 0.1 eV. Uncertainty in determining different oxidation states is found to be ± 5%

level in the lower binding energy side is mainly due to the lattice oxygen (O_L) present in the stoichiometric WO_3, while shoulder feature at the higher binding energy is due to the oxygen vacancies (O_V) present in the sub-stoichiometric tungsten oxides (WO_{3-x}). The relative percentage of oxygen vacancy is found to be around 19.2% and 21.1% for bare and silver-loaded films, respectively. By calculating the area under the curves of W 4f and O_L peaks and normalized by the relative atomic sensitivity factors and analyser transmission functions, the estimated atomic ratios of W to O are found to be around 1:2.82 for both the samples. Figure 6d shows the Ag $3d_{5/2}$ and Ag $3d_{3/2}$ spin–orbit doublet peaks centered at ~ 368.0 and ~ 374.0 eV, respectively, for silver-loaded sample. A closer view of the Ag 3d spectrum shows that silver has two charge states (i) a pair of main peak corresponds to the Ag^0 and (ii) another pair of shoulder in the higher binding energy side corresponds to the Ag^+ states. For a quantitative estimate of the relative percentage of Ag^+ states, we have fitted the spectrum with two pairs of Ag 3d spin–orbit peaks. The deconvoluted spectra show the

characteristic doublet peaks of Ag^0 components at ~ 368.0 and ~ 374.0 eV for Ag $3d_{5/2}$ and Ag $3d_{3/2}$, respectively. The shoulder doublet peaks of Ag^+ components are present at 368.3 and 374.3 eV, respectively. The relative percentage of Ag^+ components is estimated to be around 26.7% for silver-loaded sample.

The W 4f peaks of silver-loaded film shifted to higher binding energies by ~ 0.5 eV with respect to the corresponding peaks in bare film. Similarly, the O 1 s peaks of silver-loaded film were located at ~ 530.6 and 532.1 eV, associated with O_L and O_V, respectively, which are also ~ 0.5 eV higher than the corresponding peaks of the bare film. A comparison with XPS spectra of silver loaded and bare film shows the presence of the same amount of chemical shift of ~ 0.5 eV to higher binding energies in W 4f and O 1 s spectra in the silver loaded sample. However, we do not observe any peak broadening and line-shape changes in the corresponding spectra between the two samples. It turns out that a charge transfer contribution between Ag and WO_{3-x} (O 1 s and W 4f orbitals) in the Ag-loaded sample is the leading contribution to the observed chemical shift. The electron transfer help us to reduce the interfacial barrier height between Ag nanoparticles and WO_{3-x} junctions, leading to increasing the electron conduction channel.

3.2 Gas sensing performances of WO_{3-x} and Ag–WO_{3-x} films

Figure 7 demonstrates the NO_2 sensing properties of the fabricated sensors recorded at 225 °C. The sensing measurements were performed at different operating temperatures limited to 225 °C and at various gas concentrations. Due to the technical limitations of our heater, placed below the samples, the temperature cannot reach beyond 225 °C. All the measurements were performed once the resistance across the electrodes was stabilized at a fixed operating temperature in air, and then, sufficient time was given before introduction of the calibrated NO_2 gas into the chamber. The quality and statistics of our data taken at operating temperature below 225 °C were not considerably good and thus not shown here. The gas sensing response is related to the changes in electrical resistance of the device before and after the target gas is introduced into the chamber. The increase and/or decrease in resistance during the interaction of the target gas and the sensing material is the measure of the sensitivity of the device. The sensing response is a key parameter to establish the efficiency of the sensing performance, which is defined by the following formula:

$$\text{Sensing response}(\%) = \frac{|\,\text{Ra} - \text{Rg}\,|}{\text{Ra}} \times 100, \tag{2}$$

where R_a and R_g are the resistances of the gas sensors before and after the exposure the NO_2 gas at a fixed operating temperature. The as-prepared WO_{3-x} when exposed to NO_2 gas shows noticeable increase in resistance even at 1 ppm concentration. The sensing response becomes more prominent with increasing NO_2 concentration and demonstrates a sensing response of 12% recorded at 10 ppm concentration. Interestingly, the Ag-loaded WO_{3-x} films exhibit distinguishable response of 8.4% at 0.5 ppm NO_2 concentration at similar temperature of 225 °C. Moreover, Ag-loaded WO_{3-x} demonstrated NO_2 sensing response of more than 70% at 10 ppm concentration. Incorporation of Ag into the films has been found to enhance the sensing performance appreciably. The sub-ppm level NO_2 gas detection was achieved with the help of Ag nanoparticles decorated on the WO_{3-x} films. The operating temperature was varied from 100 to 225 °C, and it was observed that the highest sensing response achieved at 225 °C for both WO_{3-x} and Ag-loaded WO_{3-x} sensors. Although the resistance of Ag-loaded WO_{3-x} samples is higher compared to that of the bare films due to smaller grains and larger grain boundaries in the former case. The change in resistance upon NO_2 gas exposure in Ag–WO_{3-x} films is increased due to the catalytic effect of Ag nanoparticles. The silver loaded film exhibits a better response and recovery behavior compared with that of the bare sensor. The response and recovery time have been estimated to be 2 and 3 min for Ag-loaded film, while bare film shows 3

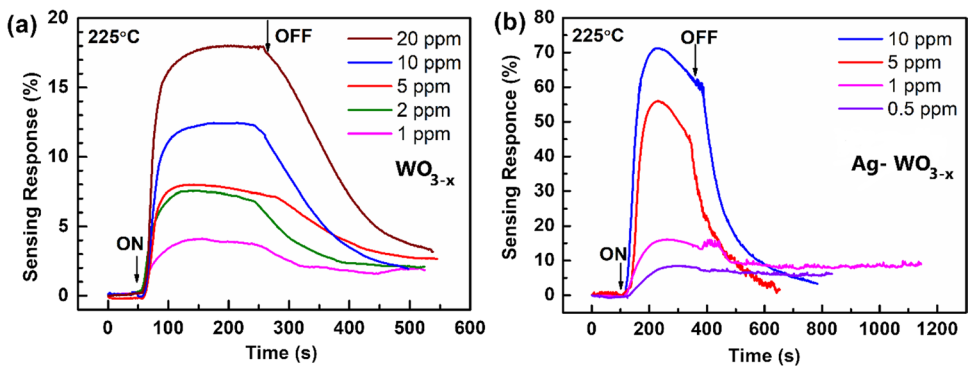

Fig. 7 **a**, **b** Sensing performance from both the films taken at 225 °C temperature. Pink, red, and blue line curves denote sensing response at 1, 5, and 10 ppm NO_2 gas concentrations, respectively. WO_{3-x} shows ~ 12% sensitivity, while Ag–WO_{3-x} shows ~ 70% sensitivity (blue line) with 10 ppm NO_2 gas concentration

Table 2 Comparison of the NO_2 gas sensing performance of our sensor and other reported sensors based on WO_3

Sensing materials	Synthesis process	Concentration (ppm)	Sensor response (%)	T_{Op} (°C)	References
Pt doped WO_3	Hydrothermal	5	81.6	150	[11]
Pt–WO_3	Hydrothermal	200	13.6	125	[19]
WO_3 nanofibres	Electrospinning	3	101.3	90	[20]
Au–WO_3	Precipitation and impregnation	5	836.6	250	[21]
Au–WO_3	Electrospinning	1	34.3	175	[22]
WS_2–WO_3	Exfoliation and sonication	5	16.7	25	[23]
La_2O_3–WO_3	Flame spray pyrolysis	5	7213.6	150	[24]
WO_3nanosheets	Dip coating	5	15.5	210	[25]
WO_3	DC magnetron sputtering	0.5	80	180	[26]
Carbon dots–WO_3	Solvothermal	0.2	1.1	18	[27]
WO_3/Si nanobelts	Chemical etching	5	3.6	25	[28]
Ag–WO_{3-x}	Reactive magnetron sputtering	0.5	8.4	225	This work

and 4 min, respectively. The NO_2 gas sensing performance of our sensors is compared with the best-reported values of the other sensors and are summarized in Table 2. Our fabricated sensor exhibits good sensing characteristic in terms of its sub-ppm level sensitivity and low detection limit, which would open up the opportunity for exploring the potential application of this materials.

In general, the resistance measured across a semiconducting metal-oxide (SMO)-based chemiresistive sensor is mainly governed by three contributions. These are (i) the electrical resistance offered by the bulk of the individual grain to electron flow, which decreases with increasing temperature, (ii) the electrical resistance across the grain boundaries of the material, which again decreases with increasing temperature, and (iii) the electrical resistance offered by the surface region of the material covering grains and grain boundaries [4, 29, 30]. The last term depends on the interaction of the SMO material surface with the oxidizing or reducing gases present in the environment, and dominates over the other two terms in the temperature range of operation. This oxidation or reduction reaction occurring over the surface of the sensing material is governed by the thermally activated process, and thus increases with increasing temperature. However, the adsorption of the gas molecules on the surface of the sensing material decreases with increasing temperature due to the higher kinetic energy imparted to the gas molecule, and thus, the effective chemical reaction significantly reduces [5, 31]. Experiment performed at the operating temperature of 225 °C clearly established the fact that the adsorption of NO_2 gas on WO_{3-x} surface is heavily increased, and thus, the sensitivity of the semiconductor films increase. With the presence of silver nanoparticles on the surface, the sensitivity further increases as evident from Fig. 7 under exactly the same operating temperature. Figure 8 shows the gas sensors stability and repeatability taken at 225 °C. The devices display no sign of degradation or drift from its original value even after 5–6 days of operation.

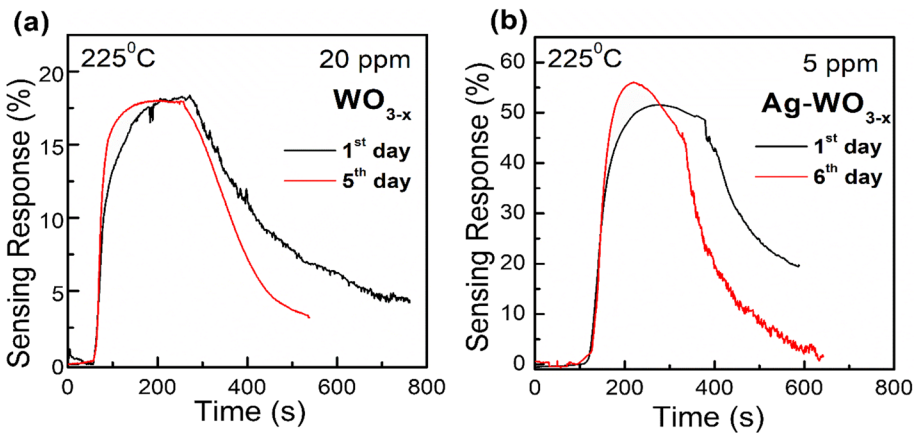

Fig. 8 **a**, **b** Stability behavior of the sensor of WO_{3-x} with 20 ppm and Ag–WO_{3-x} with 5 ppm NO_2 gas at 225 °C, respectively

3.3 *Gas sensing mechanism of WO_{3-x} and Ag–WO_{3-x} films*

Various factors, such as the nature of the target gas (reducing or oxidizing), the sensing material types (*p*-type or *n*-type), temperature etc, determine the increase or decrease in the device resistance and thus the sensitivity of the devices. When the sensing material is *n*-type and the target gas is oxidizing in nature, the device resistance increases upon interaction with the target gas [5, 32, 33]. It decreases when the material is *n*-type and the target gas is reducing in nature [2, 19, 34]. In addition, the changes in device resistance depends upon the temperature at which the device is working. Usually, the metal-oxide semiconductor sensor works at high temperature which generates more free carriers, and thereby the surface state of adsorbed oxygen changes. This intensifies the interaction between the target gas and the material, and thus improving the overall sensing performance of the device [3, 35, 36]. At room temperature, the physical or chemical process involved in sensing mechanism of a metal-oxide semiconductor gas sensor does not execute enough changes in resistance with respect to the target gas.

WO_{3-x} is an n-type semiconductor material due to the presence of free electrons generated from surface oxygen vacancies as demonstrated in our XPS studies [6, 37]. When as-prepared WO_{3-x} is exposed to ambient air, oxygen molecules in air interact with WO_{3-x} surface and are chemisorbed. This oxygen chemisorption mechanism depends heavily on sensor temperature as the sensor operating temperature decides the chemisorbed species of oxygen. These chemisorbed oxygens collect free electrons from WO_{3-x} surface itself, and thereby depleting the surface from electrons [7][20, 38]. Therefore, an electron depletion region is formed at the sensor surface, which increases its resistance in air. Any increase in temperature will vary the sensor resistance as thermally generated electrons will contribute to its conductivity as well as the chemisorption–desorption rate will be impacted with increasing temperature [8]. Since NO_2 molecules exhibit stronger electron affinity energy (220 kJ/mol) than O_2 (20 kJ/mol), they are also chemisorbed on WO_{3-x} surface. Upon chemisorption, NO_2 interacts with chemisorbed oxygen and captures their electrons causing more electron depletion from WO_{3-x} surface. This causes the sensor resistance to increase. This increase in resistance maintains a power-law relation with the density of supplied gas [9, 21]. In this study, a large change in resistance was observed at the operating temperature of 225 °C.

The experimental data demonstrated that the sensing response of the device increased after Ag incorporation, i.e., under similar NO_2 concentration, Ag–WO_{3-x} sensors exhibit higher increment in resistance. This enhancement in sensing performance is attributed to the catalytic effect of Ag nanoparticles and chemical sensitization of the WO_{3-x} nanostructures. A schematic of the sensing mechanism of WO_{3-x} and Ag–WO_{3-x} nanocrystalline thin films is demonstrated in Fig. 9. Due to the catalytic contribution of Ag nanoparticles, the number of surface adsorption sites are greatly enhanced which improves the electron-capture interaction from WO_{3-x} surface, and thereby causing more electron depletion and increase in sensor resistance. The catalytic activity of Ag nanoparticles also reduces the activation energy of electron-transfer reaction between chemisorbed NO_2 and WO_{3-x}, which eventually facilitates the formation of thicker electron depletion layer. Apart from increasing the number of chemisorbed oxygen molecules, Ag nanoparticles can also accelerate the diffusion and mobilization of the chemisorbed oxygen species onto the WO_{3-x} surface sites and capture free electrons from WO_{3-x} conduction band by conversion of gas molecules into (ions). This enhances the tendency of adsorbed oxygen species and generates more effective active adsorption sites which in turn strengthens the diffusion of NO_2 and their conversion to NO_2^- on WO_{3-x} surface. Therefore, Ag nanoparticles catalyze the ionization process of the target gas molecules. Collectively, Ag nanoparticles favor the following interactions through its catalytic activity to improve WO_{3-x} sensing performance:

(i) Reduction in electron-capture activation energy
(ii) Increasing the chemisorbed oxygen molecules
(iii) Enhancing the chemisorption of oxidizing gas on WO_{3-x} /Ag surface.
(iv) Acceleration of diffusion of oxygen molecules and NO_2 molecules on WO_{3-x} surface.

Additionally, Ag nanoparticles can amplify the sensor response through chemical sensitization and spillover effect. XPS analysis of O 1 s spectra in WO_{3-x} and Ag–WO_{3-x} samples demonstrate an enhancement in surface oxygen vacancies in Ag-loaded samples. These oxygen vacancies influence the transfer of electrons to the adsorbed NO_2 molecules that enhances the sensor response upon Ag loading. Furthermore, XPS analysis of Ag 3*d* spectra reveals the presence of a thin layer of Ag_2O on Ag nanoparticle surface. This Ag_2O layer can potentially improve the sensor response through enhanced chemical sensitization and spillover mechanism. When NO_2 gas molecules are adsorbed on Ag nanoparticles, they can collect oxygen ions from Ag_2O reducing it to Ag^0 nanoparticles and are excited to NO_3^-. The excited NO_3^- species are transferred to WO_{3-x} surface where it extracts more electrons from WO_{3-x} surface. Therefore, more electrons are depleted from sensor surface, and thereby reducing the conduction channel volume. This additional electron depletion from sensor surface causes an improved sensor performance by increasing its resistance. Reduction of the conduction channel volume have been proposed in

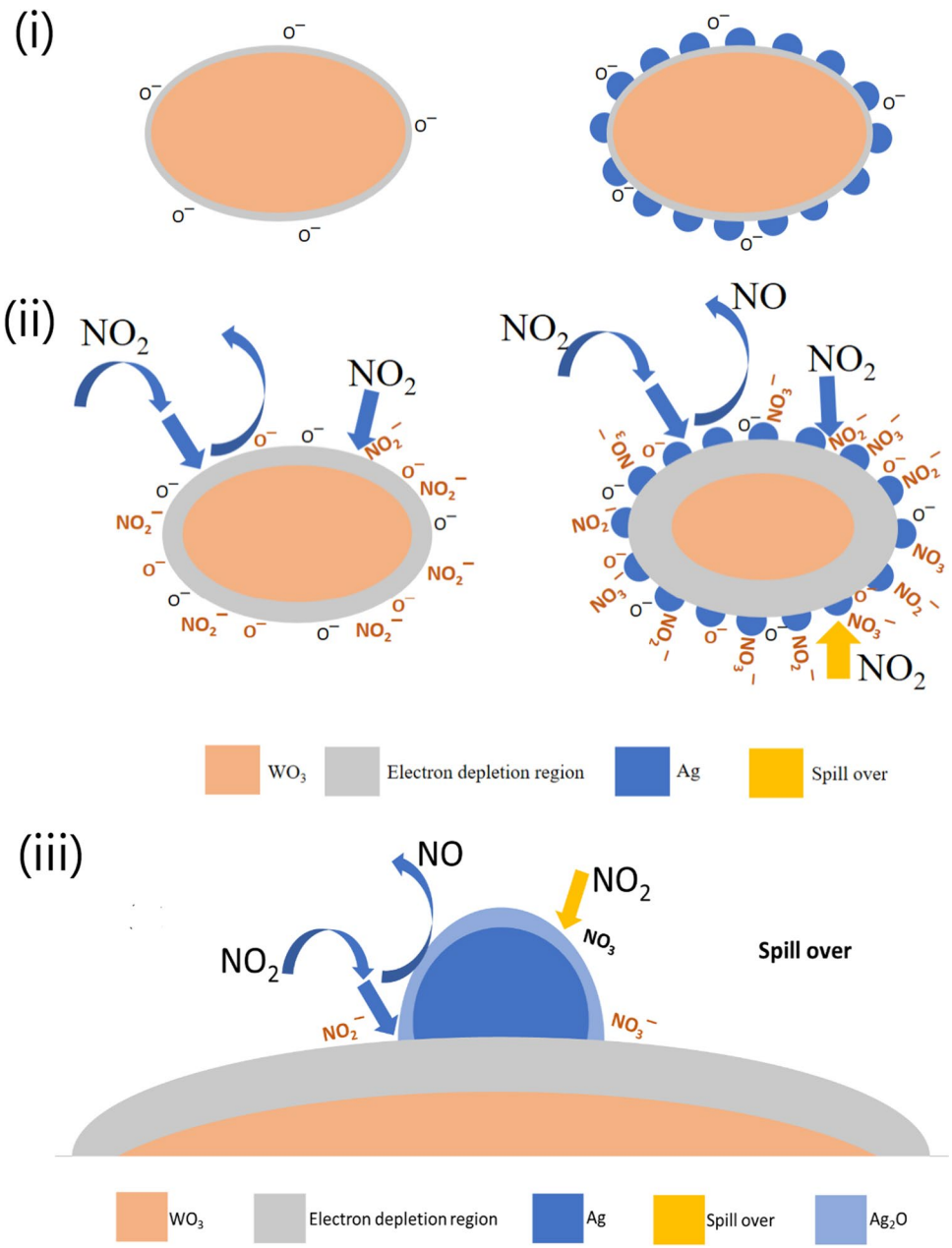

Fig. 9 **(i)** Chemisorption of O molecules from the air or any oxidizing gas. The adsorbed O molecules capture free electron from the surface and becomes O^-. **(ii)** Adsorption of NO_2 and spillover effect which turns into NO and NO_3^- enhancing the electron depletion region and thereby the sensitivity of the devices. **(iii)** Interaction of NO_2 gas with the thin Ag_2O layer formed on the surface of the Ag–WO_{3-x} film. The spillover effect enhances the electron depletion region by forming Ag^+ on the surface and increase the electrical resistance causing an increase in the sensitivity

NO_2 sensing by noble metal decorated WO_3 [22, 39, 40]. The observed chemisorption, sensitization, and desorption mechanism behind NO_2 sensing can be summarized in the following three equations:

$$NO_2(g) + e^- = NO_2^-(ads) \quad (3)$$

$$NO_2(g) + e^- = NO(g) + O^-(ads) \quad (4)$$

$$NO_2(g) + Ag_2O + e^- = NO_3^-(ads) + Ag. \quad (5)$$

It is to be noted that the sensing characteristics of WO_{3-x} and Ag-loaded WO_{3-x} exhibit dissimilar shapes as demonstrated in Fig. 7. For WO_{3-x} sensors, the sensing response increases rapidly before reaching a steady-state value and it is continued until the supply of NO_2 gas is terminated. Thus, a flat steady-state condition is achieved in the presence of the gas. However, the steady-state behavior is significantly modified in case of Ag-loaded WO_{3-x} samples. The response increases rapidly with introducing the gas and reaches the steady-state condition, and then, it gradually decreases even before terminating the gas supply. There is a noticeable decrease in sensing response before the gas supply is turned off. This reduction in sensing response may occur due to the reduction in NO_2 adsorption on WO_{3-x} surface and the presence of

Ag nanoparticles. Since the Ag-loaded WO_{3-x} has much smaller grain sizes and more number of grain boundaries, the amount of trapped NO_2 molecules at the grain boundaries after NO_2 exposure becomes considerably larger. Furthermore, these trapped NO_2 molecules may prevent further adsorption of active NO_2, and thereby reducing the response properties. Besides, at this operating temperature, the Ag^0 nanoparticles may contribute electrons to the conduction band of WO_{3-x} and change to the oxidation state of Ag^+, consistent with the XPS results. The donated electron can effectively reduce the depletion region, and thereby enhancing the channel conductivity.

4 Conclusion

We have demonstrated the synthesis of WO_{3-x} nanocrystalline thin films functionalized with Ag nanoparticles prepared by reactive ion magnetron sputtering process to achieve highly sensitive and selective NO_2 gas sensing performance. The films are characterized to be nanocrystalline in nature with spherical granular surface morphology. Surface electronic structure examined by X-ray photoelectron spectroscopy revealed the presence of an Ag_2O ultrathin layer on Ag nanoparticles, which enhances the chemical sensitization effect through spillover mechanism. Upon exposure to NO_2 gas of 10 ppm concentration, a maximum response of about 12 and 70% were observed for bare and silver-loaded WO_{3-x} films at 225 °C, respectively. A faster response and recovery time were recorded for silver-loaded films compared to that of the bare films. The results demonstrate the enhanced capability of sensing properties of Ag-loaded WO_{3-x} compared to bare WO_{3-x} nanocrystalline films prepared by PVD techniques for ultrasensitive NO_2 gas sensing applications.

Acknowledgements The authors thank Director, CSIR-CGCRI and Dr. Tarun K. Kayal for their constant encouragement and support. M. H. thanks CSIR for CSIR-NET (SRF) Fellowship. K S. acknowledges financial assistance from the DST Inspire Faculty grant (DST/INSPIRE/04/2021/004205). Authors are also thankful to the central facility, CSIR-CGCRI, and the Department of Physics, SKBU for the support of their facilities and equipments.

Author contributions MH: carrying measurements, visualization, analysis, and writing—original draft. KS: formal analysis, manuscript composition, review, and editing. AM: XPS measurements. AB: review and editing. PKK: resources. R: sensing measurements. MSK: sensing measurements, review, and editing. SB: TEM measurements. PP: conceptualization, methodology, supervision, and writing—review and editing.

Data Availability The data presented in this study will be made available on request from the corresponding author.

Declarations

Conflict of interest The authors declare no conflicts of interest in connection with this manuscript. Details on potential conflicts of interest are included under Publishing Ethics.

Ethical approval Not applicable.

References

1. J. Kukkola, J. Mäklin, N. Halonen et al., Gas sensors based on anodic tungsten oxide. Sens. Actu. B Chem. **153**, 293–300 (2011). https://doi.org/10.1016/J.SNB.2010.10.043
2. K. Wetchakun, T. Samerjai, N. Tamaekong et al., Semiconducting metal oxides as sensors for environmentally hazardous gases. Sens. Actu. B Chem. **160**, 580–591 (2011). https://doi.org/10.1016/J.SNB.2011.08.032
3. C.M. Hung, D.T.T. Le, N. Van Hieu, On-chip growth of semiconductor metal oxide nanowires for gas sensors: a review. J. Sci. Adv. Mater. Dev. **2**, 263–285 (2017). https://doi.org/10.1016/J.JSAMD.2017.07.009
4. K.Y. Ko, J.G. Song, Y. Kim et al., Improvement of gas-sensing performance of large-area tungsten disulfide nanosheets by surface functionalization. ACS Nano **10**, 9287–9296 (2016). https://doi.org/10.1021/acsnano.6b03631
5. C. Dong, R. Zhao, L. Yao et al., A review on WO_3 based gas sensors: Morphology control and enhanced sensing properties. J. Alloys Compd. **820**, 153194 (2020). https://doi.org/10.1016/J.JALLCOM.2019.153194
6. M. Akiyama, J. Tamaki, N. Miura, N. Yamazoe, Tungsten oxide based semiconductor sensor highly sensitive to NO and NO_2. Chem. Lett. **20**, 1611–1614 (1991)
7. C. Balázsi, K. Sedlácková, E. Llobet, R. Ionescu, Novel hexagonal WO_3 nanopowder with metal decorated carbon nanotubes as NO_2 gas sensor. Sens. Actu. B Chem. **133**, 151–155 (2008). https://doi.org/10.1016/j.snb.2008.02.006
8. Y. Xu, T. Ma, Y. Zhao et al., Multi-metal functionalized tungsten oxide nanowires enabling ultra-sensitive detection of triethylamine. Sens. Actu. B Chem. (2019). https://doi.org/10.1016/j.snb.2019.127042
9. Y. Lin, L. Huang, L. Chen et al., Fully gravure-printed NO_2 gas sensor on a polyimide foil using WO_3-PEDOT: PSS nanocomposites and Ag electrodes. Sens. Actu. B Chem. **216**, 176–183 (2015). https://doi.org/10.1016/j.snb.2015.04.045
10. M. Penza, C. Martucci, G. Cassano, NO_x gas sensing characteristics of WO_3 thin films activated by noble metals (Pd, Pt, Au) layers. Sens. Actu. B Chem. **50**, 52–59 (1998). https://doi.org/10.1016/S0925-4005(98)00156-7
11. T. Li, Y. Shen, X. Zhong et al., Effect of noble metal element on microstructure and NO_2 sensing properties of WO_3 nanoplates prepared from a low-grade scheelite concentrate. J. Alloys Compd. **818**, 152927 (2020). https://doi.org/10.1016/J.JALLCOM.2019.152927
12. R. Lu, X. Zhong, S. Shang et al., Effects of sintering temperature on sensing properties of WO_3 and Ag-WO_3 electrode for NO_2 sensor. R Soc. Open Sci. **5**, 171691–171701 (2018). https://doi.org/10.1098/rsos.171691
13. Y. Zhu, C. Blackman, P. Zhou et al., Facile synthesis of Ag nanoparticles-decorated WO_3 nanorods and their application in O_2 sensing. J. Alloys Compd. **936**, 167930–167943 (2023). https://doi.org/10.1016/j.jallcom.2022.167930
14. P. Jaroenapibal, P. Boonma, N. Saksilaporn et al., Improved NO_2 sensing performance of electrospun WO_3 nanofibers with silver

doping. Sens. Actu. B Chem. **255**, 1831–1840 (2018). https://doi.org/10.1016/j.snb.2017.08.199
15. L. Chen, C. Tsang, Ag doped WO_3-based powder sensor for the detection of NO gas in air. Sens. Actu. B **89**, 68–75 (2002)
16. Y. Wang, X. Cui, Q. Yang et al., Preparation of Ag-loaded mesoporous WO_3 and its enhanced NO_2 sensing performance. Sens. Actu. B Chem. **225**, 544–552 (2016). https://doi.org/10.1016/j.snb.2015.11.065
17. Sable PB, Abood NT, Botewad SN, Dharne GM (2022) Successive ion layer adsorption and reaction method developed ZnO thin films for NO_2 gas sensing. Phys. Status Solidi (A) Appl. Mate. Sci. 219:2100703–2100709. https://doi.org/10.1002/pssa.202100703
18. M. Hossain, S. Pal, S. Masanta et al., Large area planar UV–Visible photodetectors using wide bandgap WO_3−δ films. Opt. Mater. (Amst.) **135**, 113322 (2023). https://doi.org/10.1016/J.OPTMAT.2022.113322
19. Y. Wang, J. Liu, X. Cui et al., NH_3 gas sensing performance enhanced by Pt-loaded on mesoporous WO_3. Sens. Actu. B Chem. **238**, 473–481 (2017). https://doi.org/10.1016/J.SNB.2016.07.085
20. J. Zhang, D. Leng, L. Zhang et al., Porosity and oxygen vacancy engineering of mesoporous WO_3 nanofibers for fast and sensitive low-temperature NO_2 sensing. J. Alloys Compd. **853**, 157339 (2021). https://doi.org/10.1016/J.JALLCOM.2020.157339
21. S. Kabcum, N. Kotchasak, D. Channei et al., Highly sensitive and selective NO_2 sensor based on Au-impregnated WO_3 nanorods. Sens. Actu. B Chem. **252**, 523–536 (2017). https://doi.org/10.1016/j.snb.2017.06.011
22. H. Lin, J. Wang, S. Xu et al., Au-WO_3 nanowire-based electrodes for NO_2 sensing. ACS Appl. Nano Mater. **5**, 14311–14319 (2022). https://doi.org/10.1021/acsanm.2c02289
23. Y. Han, Y. Liu, C. Su et al., Hierarchical WS_2–WO_3 Nanohybrids with P-N heterojunctions for NO_2 detection. ACS Appl. Nano Mater. **4**, 1626–1634 (2021). https://doi.org/10.1021/acsanm.0c03094
24. M. Siriwalai, M. Punginsang, K. Inyawilert et al., Flame-spray-synthesized La_2O_3-loaded WO_3 nanoparticle films for NO_2 sensing. ACS Appl. Nano Mater. (2022). https://doi.org/10.1021/acsanm.2c04392
25. Y. Gui, L. Qian, K. Tian et al., In situ growth of oxygen defect-rich ultra-thin WO_3 nanosheets for ultra-fast recovery NO_2 sensors. IEEE Sens. J. (2022). https://doi.org/10.1109/JSEN.2022.3219614
26. Y. Jeong, S. Hong, G. Jung et al., Effects of oxygen gas in the sputtering process of the WO_3 sensing layer on NO_2 sensing characteristics of the FET-type gas sensor. Solid State Electron. **200**, 108563 (2023). https://doi.org/10.1016/J.SSE.2022.108563
27. W. Bian, H. Dou, X. Wang et al., Fabrication and computational study of a chemiresistive NO_2 gas sensor based on the carbon dots-WO_3 heterostructure for operating below room temperature. ACS Sens. **8**, 748–756 (2023). https://doi.org/10.1021/acssensors.2c02291
28. Y.R. Chen, Y. Chen, P.H. Chiu et al., Synergetic interplay of curved si nanobelts and WO_3 nanoparticles as heterostructure design featuring effective room-temperature NO_2 detection. ACS Appl. Nano Mater. **5**, 8962–8972 (2022). https://doi.org/10.1021/acsanm.2c01169
29. N. Ramgir, N. Datta, M. Kaur et al., Metal oxide nanowires for chemiresistive gas sensors: issues, challenges and prospects. Coll. Surf A Physicochem. Eng. Asp. **439**, 101–116 (2013). https://doi.org/10.1016/J.COLSURFA.2013.02.029
30. Y. Ding, X. Guo, Y. Zhou et al., Copper-based metal oxides for chemiresistive gas sensors. J. Mater. Chem. C Mater. **5**, 16218 (2022)
31. T. Lei, Z. Rao, S. Zhang et al., The irreversible R–T curves of metal oxide gas sensor under programmed temperature cycle. Sens. Actu. B Chem. **235**, 481–491 (2016). https://doi.org/10.1016/J.SNB.2016.05.113
32. C.H. Wu, Z. Zhu, S.Y. Huang, R.J. Wu, Preparation of palladium-doped mesoporous WO_3 for hydrogen gas sensors. J. Alloys Compd. **776**, 965–973 (2019). https://doi.org/10.1016/J.JALLCOM.2018.10.372
33. H.J. Kim, J.H. Lee, Highly sensitive and selective gas sensors using p-type oxide semiconductors: overview. Sens. Actu. B Chem. **192**, 607–627 (2014). https://doi.org/10.1016/J.SNB.2013.11.005
34. F.A. Sabah, N.M. Ahmed, Z. Hassan, H.S. Rasheed, High performance CuS p-type thin film as a hydrogen gas sensor. Sens. Actu. A Phys. **249**, 68–76 (2016). https://doi.org/10.1016/J.SNA.2016.08.026
35. Y.V. Kaneti, Z. Zhang, J. Yue et al., Crystal plane-dependent gas-sensing properties of zinc oxide nanostructures: experimental and theoretical studies. Phys. Chem. Chem. Phys. **16**, 11471–11480 (2014). https://doi.org/10.1039/c4cp01279h
36. M. Akbari-Saatlu, M. Procek, C. Mattsson et al., Nanometer-thick ZnO/SnO_2 heterostructures grown on alumina for H2S sensing. ACS Appl. Nano Mater. **5**, 6954–6963 (2022). https://doi.org/10.1021/acsanm.2c00940
37. X. Sun, C. Wang, D. Su et al., Application of photocatalytic materials in sensors. Adv. Mater. Technol. (2020). https://doi.org/10.1002/admt.201900993
38. P.V. Morais, P.H. Suman, R.A. Silva, M.O. Orlandi, High gas sensor performance of WO_3 nanofibers prepared by electrospinning. J. Alloys Compd. **864**, 158745 (2021). https://doi.org/10.1016/J.JALLCOM.2021.158745
39. D. Degler, U. Weimar, N. Barsan, Current understanding of the fundamental mechanisms of doped and loaded semiconducting metal-oxide-based gas sensing materials. ACS Sens. **4**, 2228–2249 (2019). https://doi.org/10.1021/acssensors.9b00975
40. H. Zhang, Y. Wang, X. Zhu et al., Bilayer Au nanoparticle-decorated WO3 porous thin films: On-chip fabrication and enhanced NO_2 gas sensing performances with high selectivity. Sens. Actu. B Chem. **280**, 192–200 (2019). https://doi.org/10.1016/J.SNB.2018.10.065

Terms and Conditions

Springer Nature journal content, brought to you courtesy of Springer Nature Customer Service Center GmbH (“Springer Nature”).
Springer Nature supports a reasonable amount of sharing of research papers by authors, subscribers and authorised users (“Users”), for small-scale personal, non-commercial use provided that all copyright, trade and service marks and other proprietary notices are maintained. By accessing, sharing, receiving or otherwise using the Springer Nature journal content you agree to these terms of use (“Terms”). For these purposes, Springer Nature considers academic use (by researchers and students) to be non-commercial.
These Terms are supplementary and will apply in addition to any applicable website terms and conditions, a relevant site licence or a personal subscription. These Terms will prevail over any conflict or ambiguity with regards to the relevant terms, a site licence or a personal subscription (to the extent of the conflict or ambiguity only). For Creative Commons-licensed articles, the terms of the Creative Commons license used will apply.
We collect and use personal data to provide access to the Springer Nature journal content. We may also use these personal data internally within ResearchGate and Springer Nature and as agreed share it, in an anonymised way, for purposes of tracking, analysis and reporting. We will not otherwise disclose your personal data outside the ResearchGate or the Springer Nature group of companies unless we have your permission as detailed in the Privacy Policy.
While Users may use the Springer Nature journal content for small scale, personal non-commercial use, it is important to note that Users may not:

1. use such content for the purpose of providing other users with access on a regular or large scale basis or as a means to circumvent access control;
2. use such content where to do so would be considered a criminal or statutory offence in any jurisdiction, or gives rise to civil liability, or is otherwise unlawful;
3. falsely or misleadingly imply or suggest endorsement, approval , sponsorship, or association unless explicitly agreed to by Springer Nature in writing;
4. use bots or other automated methods to access the content or redirect messages
5. override any security feature or exclusionary protocol; or
6. share the content in order to create substitute for Springer Nature products or services or a systematic database of Springer Nature journal content.

In line with the restriction against commercial use, Springer Nature does not permit the creation of a product or service that creates revenue, royalties, rent or income from our content or its inclusion as part of a paid for service or for other commercial gain. Springer Nature journal content cannot be used for inter-library loans and librarians may not upload Springer Nature journal content on a large scale into their, or any other, institutional repository.
These terms of use are reviewed regularly and may be amended at any time. Springer Nature is not obligated to publish any information or content on this website and may remove it or features or functionality at our sole discretion, at any time with or without notice. Springer Nature may revoke this licence to you at any time and remove access to any copies of the Springer Nature journal content which have been saved.
To the fullest extent permitted by law, Springer Nature makes no warranties, representations or guarantees to Users, either express or implied with respect to the Springer nature journal content and all parties disclaim and waive any implied warranties or warranties imposed by law, including merchantability or fitness for any particular purpose.
Please note that these rights do not automatically extend to content, data or other material published by Springer Nature that may be licensed from third parties.
If you would like to use or distribute our Springer Nature journal content to a wider audience or on a regular basis or in any other manner not expressly permitted by these Terms, please contact Springer Nature at

onlineservice@springernature.com